Science

AAAS

www.sciencemag.org/cgi/content/full/science.aah5178/DC1

Supplementary Material for

A fully-programmable 100-spin coherent Ising machine with all-to-all connections

Peter L. McMahon,* Alireza Marandi,* Yoshitaka Haribara, Ryan Hamerly, Carsten Langrock, Shuhei Tamate, Takahiro Inagaki, Hiroki Takesue, Shoko Utsunomiya, Kazuyuki Aihara, Robert L. Byer, M. M. Fejer, Hideo Mabuchi, Yoshihisa Yamamoto

*Corresponding author. E-mail: pmcmahon@stanford.edu (P.L.M.); marandi@stanford.edu (A.M.)

Published 20 October 2016 as *Science* First Release
DOI: 10.1126/science.aah5178

This PDF file includes:

Materials and Methods
Supplementary Text
Figs. S1 to S5
References

Supplementary Materials for *A fully-programmable 100-spin coherent Ising machine with all-to-all connections*

Peter L. McMahon,[†,*] Alireza Marandi,[†,*] Yoshitaka Haribara, Ryan Hamerly, Carsten Langrock, Shuhei Tamate, Takahiro Inagaki, Hiroki Takesue, Shoko Utsunomiya, Kazuyuki Aihara, Robert L. Byer, M. M. Fejer, Hideo Mabuchi, Yoshihisa Yamamoto

[†]These authors contributed equally to this work.

[*]To whom correspondence should be addressed;

E-mail: pmcmahon@stanford.edu or marandi@stanford.edu.

Materials and Methods

Experimental Setup Details

The high-level schematic of our experimental setup (Fig. 1) shows a 1560-nm mode-locked fiber laser with a pulse-repetition period of $T_{\text{rep}} = 10$ ns being frequency-doubled by a second-harmonic-generation (SHG) stage, to produce 780-nm pulses that synchronously pump a periodically-poled lithium niobate (PPLN) waveguide inside a fiber-ring cavity. The cavity and PPLN nonlinear medium together form a degenerate optical parametric oscillator (DOPO). The fiber-ring cavity is approximately 330 meters long, and each round trip contains exactly 160 pulses. In the absence of coupling between the pulses being introduced, this system results in the creation of 160 independent, time-division-multiplexed pulsed OPOs (*18*). The roundtrip time, i.e., the time for a single pulse in the cavity to circulate exactly once, is $T_{\text{rt}} = 160 \times T_{\text{rep}} = 1.6$ μs. Each OPO pulse represents a single spin in the Ising machine. To implement the Ising Hamiltonian,

we need to introduce couplings between the pulses. Our scheme requires only a single delay line and two optical modulators, independent of the number of spins, and is based on a real-time measurement-feedback system to electronically reproduce optical feedback signals to be injected into the cavity that arbitrarily couple the OPO pulses (*20*). A homodyne-measurement stage measures the in-phase component c_i of each OPO pulse; a feedback-calculation stage uses a field-programmable gate array (FPGA) to compute a feedback signal $\sum_j J_{ij}c_j$ using the OPO pulse measurement results from the previous roundtrip; and an injection stage creates the optical feedback signal by phase and intensity modulation of local oscillator pulses, and injects it into the cavity.

Fig. S1 illustrates the action of the measurement-feedback subsystem. Although the cavity contains 160 pulses, only 100 of them are used for computation; the remaining 60 pulses are dummy pulses. The in-phase component of each of the first 100 pulses is measured, and these measurement results, c_i ($i = 1, \ldots, 100$), are used to compute the feedback signal to be applied to the pulses in the next roundtrip. For example, the feedback applied to OPO 1 is proportional to $\sum_{j=1}^{N=100} J_{1j}c_j$, where J_{ij} are the spin-spin interaction terms that define the Ising problem to be solved. The quantity $\sum_{j=1}^{N=100} J_{1j}c_j$ is real-valued, and may be negative or positive. Its sign is used to determine whether the phase modulator in the injection path applies a 0 or a π phase shift, and the amplitude of this feedback term is used as the control signal of the intensity modulator. We note that the feedback calculation requires performing an N-dimensional vector-vector dot product every repetition period T_{rep}, which is 10 ns in our system. To implement an N-spin Ising problem, the FPGA needs to perform a calculation comprising approximately $2N$ arithmetic operations every T_{rep}. In contrast to all-optical Ising machines (*17*), which require $2(N-1)$ distinct physical modulators to implement arbitrary Ising problems, the measurement-feedback-based approach trades off optical component resources with electronic

circuit resources, and requires only 2 optical modulators for feedback, regardless of the problem size N. We note that modern FPGAs with $> 12,000$ multipliers on a single chip exist, therefore it should be feasible to construct feedback circuits for Ising machines with $N > 10^4$ spins using current technology.

Fig. S2 shows a detailed schematic of the experimental setup. The laser is a MenloSystems C-Fiber femtosecond Erbium laser with 90-fs pulse width and a 100-MHz repetition rate. The laser output is filtered using two Agiltron fiber bandpass filters, and this light is amplified using a PriTel EDFA. There are three different phase-stabilization control loops in the setup, where each PID controller is a TEM Messtechnik LaseLock. The cavity length is stabilized via measurement of the OPO pulse amplitude. The local oscillator (LO) path to the homodyne detector is stabilized via readout of one of the two photodetectors. The injection path is stabilized via readout of the interference signal on the free port of the injection fiber beamsplitter.

The OPO pump is generated via Second Harmonic Generation in a Covesion MgO:PPLN crystal, mounted in a Covesion PV40 oven. A Covesion PV40 oven is also used to control the temperature of the custom PPLN waveguide that forms part of the OPO. All electro-optic modulators are also based on $LiNbO_3$, and were obtained from EOSPACE.

The OPO is operated in the degenerate regime (i.e., the signal and idler wavelengths are identical). It has a threshold (when the injection port is blocked) $P_{\rm th} \approx 210\,\mu$W. This value drifts between $200\,\mu$W and $215\,\mu$W on a timescale of hours to days.

The homodyne balanced photodetector is a Thorlabs PDB480C-AC with 1.6-GHz bandwidth. The FPGA module is a BEEcube miniBEE (containing one Xilinx Virtex 6 SX475T

chip, clocked at 200 MHz) with an FMC101 ADC/DAC board (containing one Maxim 19692 12-bit 2.3-GSa/sec DAC and one TI ADS 12-bit 1-GSa/sec ADC, both clocked at 800 MHz). The reason we have 60 dummy pulses in the cavity containing 160 pulses is so that the FPGA feedback signal has time to propagate so that it can be applied to the next roundtrip, with no further delay.

Supplementary Text

Further Discussion of Experimental Results

In Fig. 4A, we note that there is little variation in the success probabilities for each graph size, typically less than a factor of two. The probability of obtaining a ground state decays exponentially with graph size, falling to an average of $1.4 \pm 0.70\%$ when $N = 100$. However, we can also consider approximate solutions, and there is a very strong dependence of the success probability on the desired accuracy of the solution: the probability of finding a solution with a 95% or higher cut value of the global optimum in a single run is still on average greater than 50% for $N = 100$, and solutions with accuracy of at least 90% occur with 100% probability for $N = 100$.

In Fig. 4E, we can see that very sparse graphs are easily solved: those with $|E| = 50$ edges ($d \approx 0.01$) have an average success probability of greater than 40%, even when requiring a solution accuracy of 100%. For solution accuracies of up to 99%, the machine is able to find answers for graphs of essentially any density with reasonable success probability. The success probabilities for $\geq 90\%$-density graphs can be even higher, and are artificially reduced in this study due to the limitations of the laser control in the present experimental setup (see the Numerical Calculations section).

In Figs. 2, 3 and 4, we have presented the results from the investigation of several thousand problem instances ranging in size from $N = 8$ to $N = 100$ spins. We started off by showing that our system is able to solve every possible cubic graph instance with $N = 16$ with success probability $> 20\%$. We showed several scaling results for cubic graphs, most important of which is that high-quality approximate solutions can be obtained with computation times that appear to scale favorably, and there is a smooth tradeoff between total computation time and the accuracy of the solution. For random (non-cubic) graphs, in the vast majority of cases we were able to obtain a ground state solution, and otherwise an approximate solution with high probability. The sampling behavior we observed, yielding approximate solutions, is suggestive that measurement-feedback-based OPO Ising machines may also find a role as physical Boltzmann samplers (*31, 32*).

Benchmarking relatively small Ising problem instances is fraught with difficulty (*12*), and it is not even particularly obvious what benchmarks are appropriate in any given situation. We have not attempted to perform a systematic comparison of our experiments with classical solution methods in this paper (see the accompanying paper by Inagaki *et al.*). Nevertheless it is interesting to highlight a few data points. The BiqMac MAX-CUT solver (*33*) is a leading classical exact solver, and it took over $1,000$ sec (on the official BiqMac server with an Intel Xeon E5-2630 2.4-GHz CPU) to solve some of the $N = 100$ random graphs with $d < 0.5$ in Fig. 4E, whereas the computing time for the OPO Ising machine was < 50 ms to find an exact solution with 99% probability. This OPO-Ising-machine computation time does not include the time to transfer data into or out of the FPGA, nor to stabilize the optical setup, and only represents the time taken during the actual processing that the machine performs, but nevertheless this result suggests that the machine is already doing something computationally non-trivial. For practical

purposes, it is more appropriate to compare a classical heuristic solver against the OPO Ising machine, rather than an exact solver. The best heuristic MAX-CUT solver we are aware of (at least for problems with $N \leq 100$) is Breakout Local Search (BLS) (*34*). BLS typically finds ground-state solutions for $N = 100$ graphs within a few hundred milliseconds (on an Intel Core i7-4510U 2.6-GHz CPU), but we observed that in approximately one out of every five runs it takes longer than one second to return a good solution. In terms of only the computation time (not the wall-clock time), our machine outperforms BLS in these special cases. Even for typical runs of BLS on $N = 100$ instances, the OPO Ising machine's computation time compares favorably. However, if the overhead from other contributions to the wall-clock time, such as data transfer, are considered, then an OPO Ising machine will likely need to handle problems larger than $N = 100$ in order to be competitive with, or offer a definitive performance advantage over, the best classical heuristic solvers. For example, there are many benchmark problems with $N = 800$ vertices that BLS requires tens-to-hundreds of seconds to solve (*34*), so a speedup on instances of this size may be possible even when large overheads are taken into account.

In the case of recent experimental investigations of quantum annealers, there has been controversy about the operating regime and mechanism (*11, 13, 35*), and about whether the class of machines being considered has already delivered a speedup or will ever deliver a speedup (*12, 36–42*). Competition between various groups trying to find evidence of speedup on D-Wave quantum annealers and groups designing or modifying classical solvers to perform even better has been underway for several years. The ensuing conversations have helped to define standards for how to measure speedup of combinatorial optimizations on non-von-Neumann-architecture machines, but despite these years of effort, the central questions about the promise of quantum annealers remain open. We believe that the results in our paper indicate that coherent Ising machines merit further investigation as accelerators of combinatorial optimizations,

and we look forward to interaction with the community to try to fully understand the nature and capability of this class of optimization processor. Rigorous comparisons with the best classical solvers, and as appropriate with quantum annealers and other non-classical approaches, will be crucial future work as we increase the size of the problems that coherent Ising machines can solve.

Numerical Calculations

Several numerical models have been developed to understand the operation of networks of coupled OPOs (*17, 20, 43, 44*). In this section we summarize the model used in Ref. (*20*), and present results of simulations showing that this model fairly accurately captures the behavior of our experimental system.

Model setup The behavior of a coherent Ising machine can be modeled as c-number stochastic differential equations governing the complex amplitude (c_j, s_j) of each DOPO:

$$\mathrm{d}c_j = [(-1+p-c_j^2-s_j^2)c_j + \xi(t)\sum_i J_{ij}\tilde{c}_i]\mathrm{d}t + \frac{1}{A_\mathrm{s}}\sqrt{c_j^2+s_j^2+\frac{1}{2}}\mathrm{d}W_{c_j}, \quad (1)$$

$$\mathrm{d}s_j = (-1-p-c_j^2-s_j^2)s_j\mathrm{d}t + \frac{1}{A_\mathrm{s}}\sqrt{c_j^2+s_j^2+\frac{1}{2}}\mathrm{d}W_{s_j}. \quad (2)$$

Here, p is the pump rate, and is normalized to 1 at threshold; $\xi(t)$ is the time-dependent coupling coefficient; J_{ij} are the entries of the J matrix specifying the problem instance; A_s is a saturation parameter (corresponding to the steady-state amplitude), and $\tilde{c}_i$ denotes the measured in-phase signal amplitudes used in the feedback calculations.

In our simulations, the OPO gain in the PPLN waveguide, the out-coupling loss in the fiber

beamsplitter for the measurement subsystem, and the out-coupling loss at the injection port are taken into account as follows:

$$\mathrm{d}c_j = [(p - c_j^2 - s_j^2)c_j]\,\mathrm{d}t + \frac{1}{A_\mathrm{s}}\sqrt{c_j^2 + s_j^2 + \frac{1}{2}}\mathrm{d}W_{c_j}, \tag{3}$$

$$c_j(t) \mapsto \sqrt{1 - T_\mathrm{mes}}c_j(t) + \sqrt{T_\mathrm{mes}}\frac{f_j}{A_\mathrm{s}}, \tag{4}$$

$$c_j(t) \mapsto \sqrt{1 - T_\mathrm{inj}}c_j(t) + \sqrt{T_\mathrm{inj}}\xi(t)\sum_i J_{ij}\tilde{c}_i, \tag{5}$$

where T_mes and T_inj are the transmittances of the measurement and injection port beamsplitters respectively, and f_j is vacuum (quantum) noise added from the open port of the measurement beamsplitter. We assume a pump rate $p = 0.88$ and coupling coefficient $\xi(t) = -0.001t$, based on estimates from the experiments.

Simulation results Fig. S3, A and B, shows the in-phase amplitude of the OPOs and the cut value as a function of the cavity roundtrip number, respectively, when solving the Möbius Ladder graph with $N = 16$. These are remarkably consistent with the data obtained in the experiment, shown in Fig. 2, B and C.

We also simulated solving MAX-CUT on all $|V| = N = 16$ cubic graphs (4060 instances), just as was done in the experiments. The number of roundtrips was set to $N_\mathrm{rt} = 300$ and we performed 100 runs for each instance. Fig. S4A shows a histogram of the success probabilities for finding a ground state in a single run. In Fig. S4B, the same data are plotted to show the correlation of the success probability for each instance. Pearson's correlation coefficient between the simulation and experimental data is $r = 0.80$. The simulation captures the experimental behavior reasonably accurately. At least part of the discrepancy between the simulation and experimental results is due to the fact that the phase stabilization in the experimental setup is

imperfect. Improving the phase stability increases the success probabilities, which brings the experimental data into closer agreement with the simulation data.

The final simulation is for random graphs with $N = 100$ vertices. Fig. S5 shows how the success probability changes as a function of the pump power, and can be compared to Fig. 4E. In our experiments the pump power was restricted to $p_{\rm comp} < 1.0 \cdot p_{\rm th}$, i.e., $p < 1.0$ in the normalized simulation notation, due to limitations in our EOM control. This figure shows that even better experimental results are expected for dense graphs if the system is modified to allow $p_{\rm comp} > 1.0 \cdot p_{\rm th}$. In particular, when $p_{\rm comp} = 1.2 \cdot p_{\rm th}$, nearly every run on a dense graph results in a solution with 99% accuracy or higher.

Computational Mechanism Intuition

In this section we summarize some intuition for a quantum interpretation of the mechanism by which coherent Ising machines may solve optimization problems. This summary is based on Refs. (*20, 43*).

Four computational steps Let us assume the pumping power to the DOPO network is gradually and linearly increased from below to above the oscillation threshold. Immediately after the pump power is switched on, each DOPO is at far below the oscillation threshold, where the DOPO field is in an independent squeezed vacuum state, which can be expressed as a superposition of the 0-phase state and the π-phase state:

$$|\psi_0\rangle = \frac{1}{2}(|0{-}\mathrm{phase}\rangle + |\pi{-}\mathrm{phase}\rangle), \tag{6}$$

where

$$|0-\text{phase}\rangle = C_0|0\rangle + C_1|1\rangle + C_2|2\rangle + C_3|3\rangle + \cdots, \quad (7)$$

$$|\pi-\text{phase}\rangle = C_0|0\rangle - C_1|1\rangle + C_2|2\rangle - C_3|3\rangle + \cdots. \quad (8)$$

Here the probability amplitudes of even-photon-number states $|2n\rangle$ are given by

$$C_{2n} = [1-\tanh^2(r)]^{1/4}\frac{\sqrt{(2n)!}}{2^n n!}[\tanh(r)]^n, \quad (9)$$

and r is the squeezing parameter (*45*). Note that the $|0-\text{phase}\rangle$ and $|\pi-\text{phase}\rangle$ states resemble the Pegg-Barnett phase eigenstates (*46*) but they are not orthogonal to each other, because the probability amplitudes C_{2n} are not constant but monotonically decrease with n. Nevertheless, N DOPO fields in independent squeezed vacuum states can represent 2^N solution states simultaneously. A quantum parallel search for a solution state is implemented in this way.

Soon after turning on the pump, the initially-constant 2^N probability amplitudes for all spin eigenstates are either amplified or deamplified, depending on whether the mutual coupling among DOPO fields (Ising spin coupling) imposes either constructive interference or destructive interference. The probability amplitudes of solution states (ground states of the problem Hamiltonian) are amplified, while the probability amplitudes of non-solution states are deamplified. This step can be called quantum filtering, during which the average photon number per DOPO is still smaller than one and the DOPO phase transition has no contribution yet.

When the pumping power approaches the DOPO threshold, one particular ground state is selected as the oscillation mode while all the other ground states are suppressed. This is a spontaneous symmetry breaking process associated with the second-order phase transition. The amplified probability amplitudes of the ground states in the quantum filtering stage play an es-

sential role as the preparation step toward the successful state selection in this decision-making process. It is at this point that the quantum coherence between the degenerate ground states starts decreasing and the density operator approaches a statistical mixture.

Finally, when the pumping power exceeds the DOPO threshold, the selected ground state saturates the DOPO gain by stimulated emission and completely suppresses all the other states including the non-selected ground states. The quantum coherence among the degenerate ground states is completely lost. A quantum-to-classical crossover is completed at this point.

Fig. 9 in Ref. (*43*) shows the probabilities of obtaining one of the two degenerate ground states, $|\uparrow\downarrow\uparrow\downarrow\cdots\downarrow\rangle$ for the $N = 16$ anti-ferromagnetically coupled 1D Ising ring, versus the evolution time. Here r is the squeezing parameter for a field injected into the open port of the 90/10 output coupler. With increasing r, the accuracy of the quantum measurement of the in-phase amplitude $\hat{x} = \frac{1}{2}(\hat{a} + \hat{a}^{\dagger})$ is improved and the noise injected into the same observable of the internal field is suppressed. The total number of spin eigenstates for this problem is $2^{16} \simeq 10^5$, so the success probability for a random guess is $\sim 10^{-5}$. The quantum filtering step, just before spontaneous symmetry breaking occurs, enhances the success probability to $\sim 10^{-4}$, $\sim 10^{-3}$ and $\sim 5 \times 10^{-3}$ for $r = 0$ (vacuum state input), $r = 0.5$ and $r = 1.0$ (squeezed vacuum state input), respectively. This first increase in the success probability due to constructive interference is followed by a second increase in the success probability due to the stimulated emission associated with the DOPO phase transition.

Protection from thermal excitations If the oscillation frequency ω of a DOPO is not large compared to the temperature T of the environment, the reservoir field cannot be considered as

a quantum mechanical ground state (vacuum state). In this case, the thermal excitation injected into the internal field from the open port is expected to destroy the superposition of the 0-phase state and π-phase state, and the abovementioned quantum filtering will not function properly. The system becomes a classical oscillator network.

Fig. 13 in Ref. (*43*) shows the success probability for the $N = 16$ anti-ferromagnetically coupled 1D Ising ring problem versus the normalized pump rate, where an abrupt pumping scheme is assumed. When the average thermal photon number $n_{\rm th} \ll 1$, the optimal pump rate is just above the oscillation threshold. If the pump rate is below the threshold, the spontaneous symmetry breaking and quantum-to-classical crossover do not occur. If the pump rate is well above the threshold, the DOPO network does not spend enough time below the threshold employing the quantum filtering process. As expected, the maximum success probability at the optimum pump rate starts decreasing as the average thermal photon number, $n_{\rm th} = (e^{\hbar\omega/k_{\rm B}T} - 1)^{-1}$, exceeds one. For the experiment in our Report, $T \approx 300$ K and $\omega = 2\pi\times200$ THz, so the thermal photon number is $n_{\rm th} = 0.02$.

Previous work on OPO Ising machines

Initial experiments with optical-delay-line-coupled OPOs have demonstrated that they can find solutions to three specific Ising problems: a complete graph with $N = 4$ spins (*18*); a Möbius-Ladder graph with $N = 16$ spins (*24*); or a 1D Ising spin chain at large scale (*25*). However, none of the previous experiments were reprogrammable: they were purpose-built experiments that realized only a single problem instance each. Furthermore, they exclusively implemented graphs with a regular structure in which every node was connected in the same way. A machine with $N - 1$ delay lines and $2(N - 1)$ modulators can represent arbitrary graphs (*18, 20*), but even this linear scaling of resources renders such machines difficult and expensive to implement

for large N.

Miscellanea

A proof that MAX-CUT on cubic graphs is APX-complete appears in Ref. (*47*). APX-completeness of MAX-CUT implies that MAX-CUT is NP-complete (*48*).

To generate random cubic graphs for the benchmarks presented in Fig. 4, we used the pairing model method due to Bollobás (*49*), as explained in Ref. (*50*). To generate random graphs with fixed numbers of edges, we used the library *Matlab Tools for Network Analysis* by Gergana Bounova (*51*). Exhaustive search was used to find the ground states of the $N = 16$ cubic graphs. We used the BiqMac MAX-CUT solver (*33*) to compute the ground states of all the cubic graphs with $N > 16$. We used multiple runs of the Breakout Local Search solver (*34*) to find putative ground states of the random non-cubic, fixed-edge-number $N = 100$ graphs, with spot checks performed on $\sim 10\%$ of the instances using BiqMac.

Our 100-spin machine already has 10^4 spin-spin connections. However, 10,000-spin coherent Ising machines (using measurement feedback) should be constructable with present technology, and such machines would have 10^8 spin-spin connections – far beyond what is considered possible for current approaches to constructing quantum annealers, and challenging to achieve even in classical CMOS annealers (*52*). We also note that the recent development of micron-scale DOPOs (*53*) opens up the possibility of constructing on-chip OPO Ising machines, and our results provide impetus for such efforts.

Munro and Reid (*29*) analyzed the result of coupling the signal mode of a DOPO to a

squeezed bath. This work was extended by Maruo *et al.* (*43*) to the case of Ising machines based on DOPOs, and predicts that if squeezed vacuum states are injected into the open port of the measurement outcoupling beamsplitter, the success probability for solving Ising problem instances will be increased.

Building on two theoretical results (*30, 54*), a time-division-multiplexed boson-sampling (*55*) experiment has recently been carried out (*56*). A proposal for a boson-sampling-like experiment using squeezed states (*57*) also motivates work on multiplexed OPO systems, which can produce squeezed states (*58*).

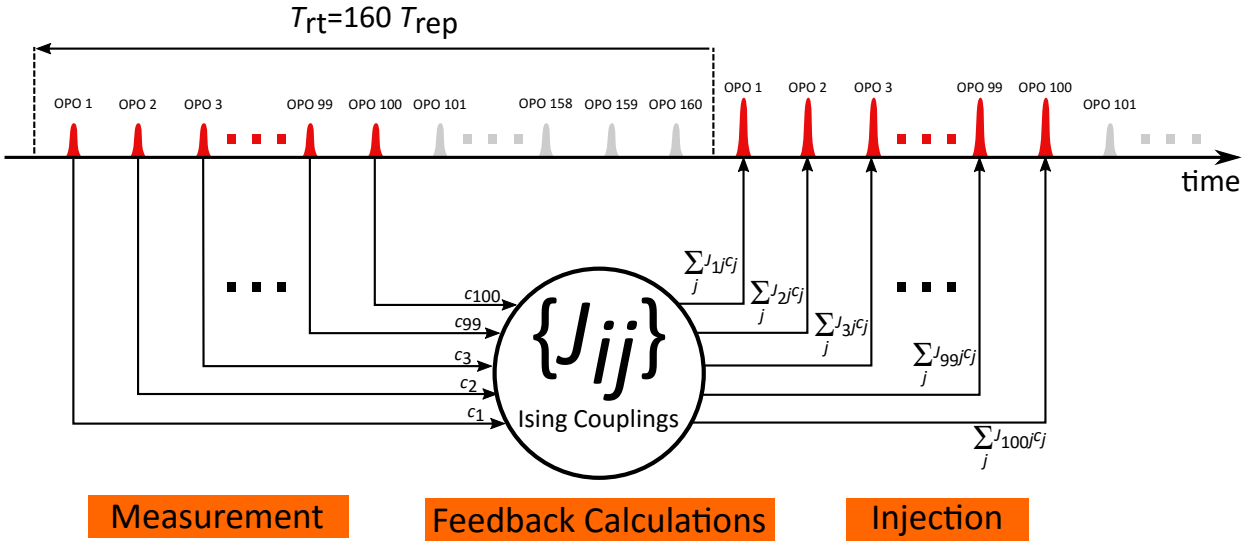

Figure S1: For each pulse i in the cavity, an N-dimensional vector-vector dot-product $\sum_{j=1}^{N=100} J_{ij}c_j$ is computed using the in-phase component c_j of every pulse from the previous roundtrip. This result is used to create the optical feedback signal.

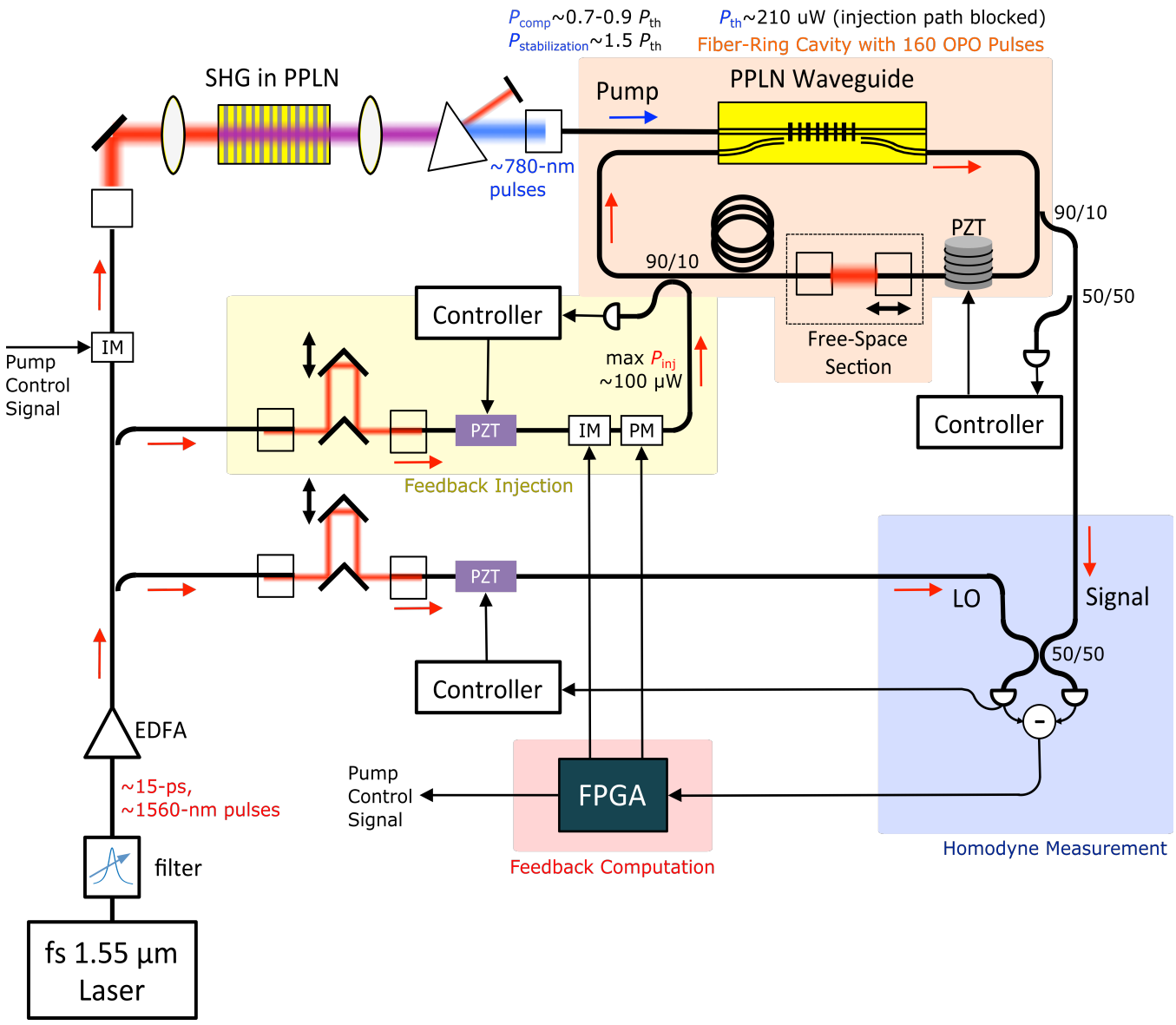

Figure S2: Detailed experimental setup schematic.

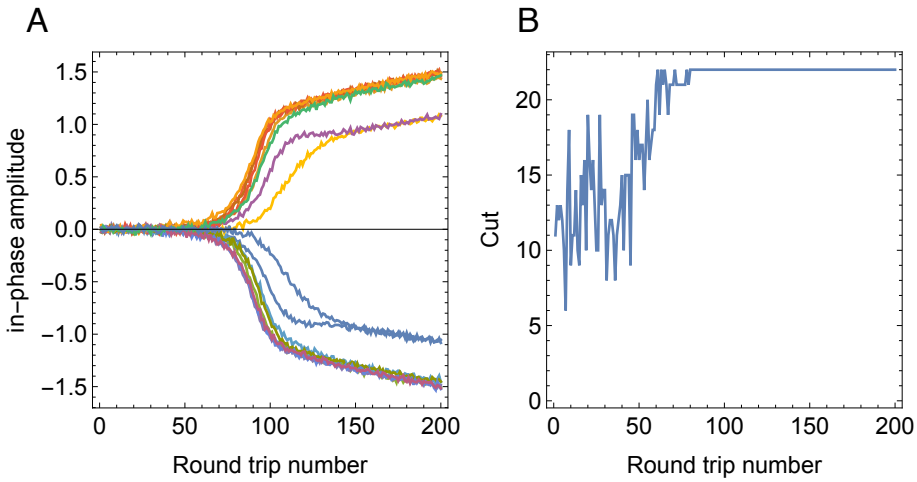

Figure S3: (**A**) In-phase amplitude of the OPO and (**B**) the number of cut when solving the Möbius ladder graph of the number of vertices $N = 16$.

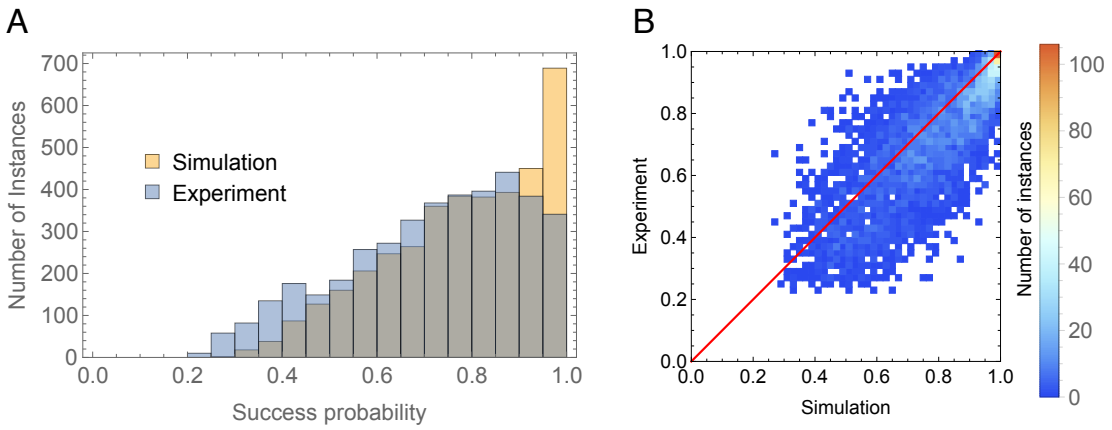

Figure S4: (**A**) Histogram of success probabilities for finding a ground state in a single run for all $N = 16$ cubic graphs. (**B**) Correlation histogram on the same data, and those from the physical experiments.

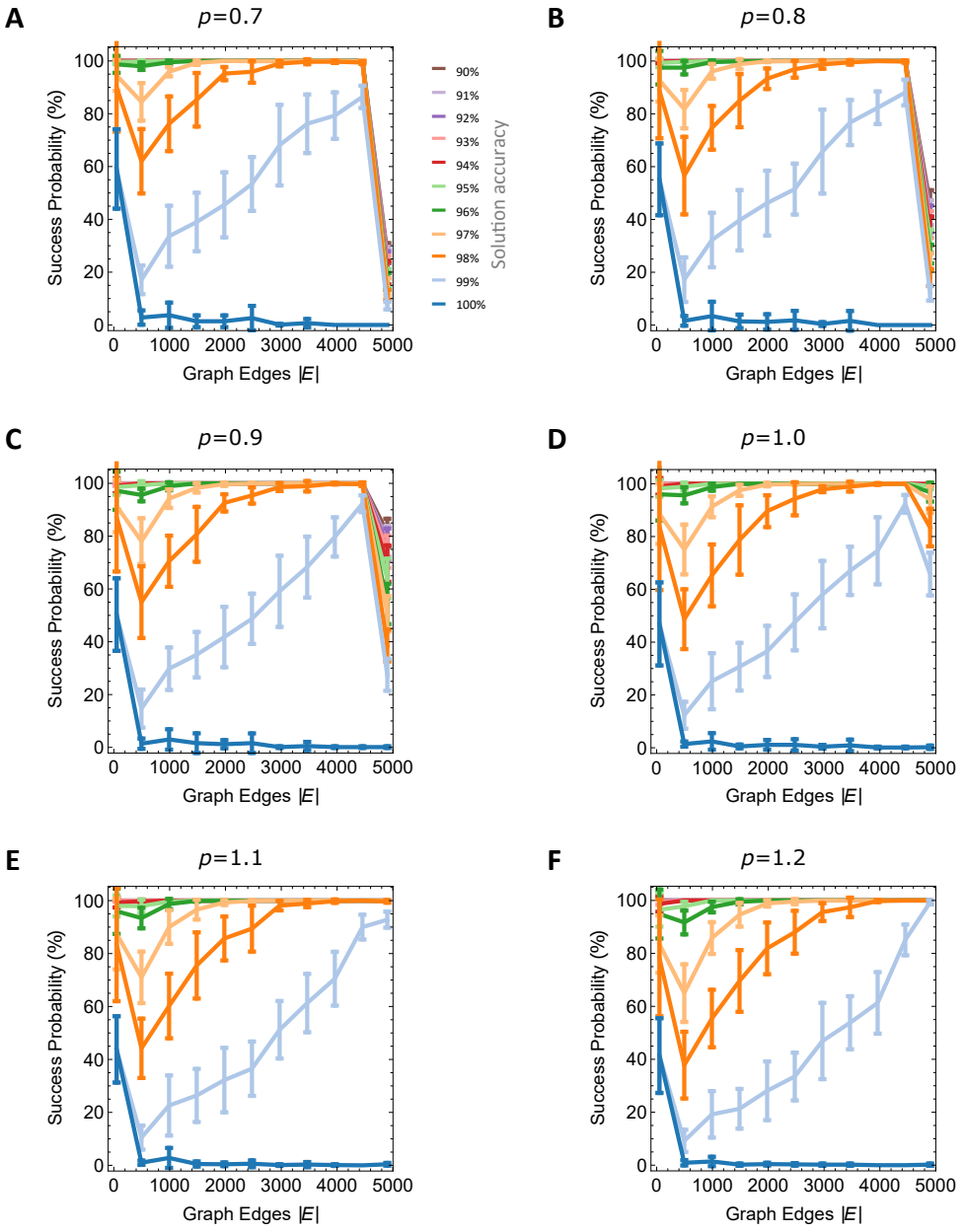

Figure S5: Plots of success probability versus number of graph edges (graph density) for the same random graphs used to generate Fig. 4E. Each plot is for a different pump power, from $0.7p_{\mathrm{th}}$ to $1.2p_{\mathrm{th}}$.

References and Notes

1. J. J. Hopfield, D. W. Tank, Computing with neural circuits: A model. *Science* **233**, 625–633 (1986). Medline doi:10.1126/science.3755256

2. D. Tank, J. Hopfield, Simple 'neural' optimization networks: An A/D converter, signal decision circuit, and a linear programming circuit. *IEEE Trans. Circ. Syst.* **33**, 533–541 (1986). doi:10.1109/TCS.1986.1085953

3. L. M. Adleman, Molecular computation of solutions to combinatorial problems. *Science* **266**, 1021–1024 (1994). Medline doi:10.1126/science.7973651

4. R. J. Lipton, DNA solution of hard computational problems. *Science* **268**, 542–545 (1995). Medline doi:10.1126/science.7725098

5. R. S. Braich, N. Chelyapov, C. Johnson, P. W. K. Rothemund, L. Adleman, Solution of a 20-variable 3-SAT problem on a DNA computer. *Science* **296**, 499–502 (2002). Medline doi:10.1126/science.1069528

6. M. Ercsey-Ravasz, Z. Toroczkai, Optimization hardness as transient chaos in an analog approach to constraint satisfaction. *Nat. Phys.* **7**, 966–970 (2011). doi:10.1038/nphys2105

7. L. Qian, E. Winfree, J. Bruck, Neural network computation with DNA strand displacement cascades. *Nature* **475**, 368–372 (2011). Medline doi:10.1038/nature10262

8. E. Farhi, J. Goldstone, S. Gutmann, J. Lapan, A. Lundgren, D. Preda, A quantum adiabatic evolution algorithm applied to random instances of an NP-complete problem. *Science* **292**, 472–475 (2001). Medline doi:10.1126/science.1057726

9. T. Kadowaki, H. Nishimori, Quantum annealing in the transverse Ising model. *Phys. Rev. E Stat. Phys. Plasmas Fluids Relat. Interdiscip. Topics* **58**, 5355–5363 (1998). doi:10.1103/PhysRevE.58.5355

10. J. Brooke, D. Bitko, T. F. Rosenbaum, G. Aeppli, Quantum annealing of a disordered magnet. *Science* **284**, 779–781 (1999). Medline doi:10.1126/science.284.5415.779

11. M. W. Johnson, M. H. Amin, S. Gildert, T. Lanting, F. Hamze, N. Dickson, R. Harris, A. J. Berkley, J. Johansson, P. Bunyk, E. M. Chapple, C. Enderud, J. P. Hilton, K. Karimi, E. Ladizinsky, N. Ladizinsky, T. Oh, I. Perminov, C. Rich, M. C. Thom, E. Tolkacheva, C. J. Truncik, S. Uchaikin, J. Wang, B. Wilson, G. Rose, Quantum annealing with manufactured spins. *Nature* **473**, 194–198 (2011). Medline doi:10.1038/nature10012

12. T. F. Rønnow, Z. Wang, J. Job, S. Boixo, S. V. Isakov, D. Wecker, J. M. Martinis, D. A. Lidar, M. Troyer, Defining and detecting quantum speedup. *Science* **345**, 420–424 (2014). Medline doi:10.1126/science.1252319

13. S. Boixo, T. F. Rønnow, S. V. Isakov, Z. Wang, D. Wecker, D. A. Lidar, J. M. Martinis, M. Troyer, Evidence for quantum annealing with more than one hundred qubits. *Nat. Phys.* **10**, 218–224 (2014). doi:10.1038/nphys2900

14. R. Barends, A. Shabani, L. Lamata, J. Kelly, A. Mezzacapo, U. Las Heras, R. Babbush, A. G. Fowler, B. Campbell, Y. Chen, Z. Chen, B. Chiaro, A. Dunsworth, E. Jeffrey, E. Lucero, A. Megrant, J. Y. Mutus, M. Neeley, C. Neill, P. J. O'Malley, C. Quintana, P. Roushan, D. Sank, A. Vainsencher, J. Wenner, T. C. White, E. Solano, H. Neven, J. M. Martinis,

Digitized adiabatic quantum computing with a superconducting circuit. *Nature* **534**, 222–226 (2016). Medline doi:10.1038/nature17658

15. P. I. Bunyk, E. M. Hoskinson, M. W. Johnson, E. Tolkacheva, F. Altomare, A. J. Berkley, R. Harris, J. P. Hilton, T. Lanting, A. J. Przybysz, J. Whittaker, Architectural Considerations in the Design of a Superconducting Quantum Annealing Processor. *IEEE Trans. Appl. Supercond.* **24**, 1–10 (2014). doi:10.1109/TASC.2014.2318294

16. E. G. Rieffel, D. Venturelli, B. O'Gorman, M. B. Do, E. M. Prystay, V. N. Smelyanskiy, A case study in programming a quantum annealer for hard operational planning problems. *Quant. Inform. Process.* **14**, 1–36 (2014). doi:10.1007/s11128-014-0892-x

17. Z. Wang, A. Marandi, K. Wen, R. L. Byer, Y. Yamamoto, Coherent Ising machine based on degenerate optical parametric oscillators. *Phys. Rev. A* **88**, 063853 (2013). doi:10.1103/PhysRevA.88.063853

18. A. Marandi, Z. Wang, K. Takata, R. L. Byer, Y. Yamamoto, Network of time-multiplexed optical parametric oscillators as a coherent Ising machine. *Nat. Photonics* **8**, 937–942 (2014). doi:10.1038/nphoton.2014.249

19. K. Takata, A. Marandi, Y. Yamamoto, Quantum correlation in degenerate optical parametric oscillators with mutual injections. *Phys. Rev. A* **92**, 043821 (2015). doi:10.1103/PhysRevA.92.043821

20. Y. Haribara, S. Utsunomiya, Y. Yamamoto, Computational Principle and Performance Evaluation of Coherent Ising Machine Based on Degenerate Optical Parametric Oscillator Network. *Entropy* **18**, 151 (2016). doi:10.3390/e18040151

21. F. Barahona, On the computational complexity of Ising spin glass models. *J. Phys. Math. Gen.* **15**, 3241–3253 (1982). doi:10.1088/0305-4470/15/10/028

22. S. Istrail, *Proceedings of the Thirty-second Annual ACM Symposium on Theory of Computing*, STOC (2000), pp. 87–96.

23. A. Lucas, Ising formulations of many NP problems. *Front. Phys.* **2**, 5 (2014). doi:10.3389/fphy.2014.00005

24. K. Takata *et al*., *Sci. Rep.* **6**, 340897 (2016).

25. T. Inagaki, K. Inaba, R. Hamerly, K. Inoue, Y. Yamamoto, H. Takesue, Large-scale Ising spin network based on degenerate optical parametric oscillators. *Nat. Photonics* **10**, 415–419 (2016). doi:10.1038/nphoton.2016.68

26. Materials and methods are available as supplementary materials on *Science* Online.

27. M. R. Garey, D. S. Johnson, L. Stockmeyer, Some simplified NP-complete graph problems. *Theor. Comput. Sci.* **1**, 237–267 (1976). doi:10.1016/0304-3975(76)90059-1

28. J. Roslund, R. M. de Araújo, S. Jiang, C. Fabre, N. Treps, Wavelength-multiplexed quantum networks with ultrafast frequency combs. *Nat. Photonics* **8**, 109 (2014). doi:10.1038/nphoton.2013.340

29. W. J. Munro, M. D. Reid, Transient macroscopic quantum superposition states in degenerate parametric oscillation using squeezed reservoir fields. *Phys. Rev. A* **52**, 2388 (1995). doi:10.1103/PhysRevA.52.2388

30. K. R. Motes, A. Gilchrist, J. P. Dowling, P. P. Rohde, Scalable boson sampling with time-bin encoding using a loop-based architecture. *Phys. Rev. Lett.* **113**, 120501 (2014). Medline doi:10.1103/PhysRevLett.113.120501

31. M. Denil, N. de Freitas, *NIPS Deep Learning and Unsupervised Feature Learning Workshop* (2011).

32. V. Dumoulin, I. J. Goodfellow, A. Courville, Y. Bengio, *arXiv:1312.5258* (2013).

33. F. Rendl, G. Rinaldi, A. Wiegele, Solving Max-Cut to optimality by intersecting semidefinite and polyhedral relaxations. *Math. Program.* **121**, 307–335 (2008). doi:10.1007/s10107-008-0235-8

34. U. Benlic, J.-K. Hao, Breakout Local Search for the Max-Cutproblem. *Eng. Appl. Artif. Intell.* **26**, 1162–1173 (2013). doi:10.1016/j.engappai.2012.09.001

35. S. W. Shin, G. Smith, J. A. Smolin, U. Vazirani, *arXiv:1401.7087* (2014).

36. A. Perdomo-Ortiz, N. Dickson, M. Drew-Brook, G. Rose, A. Aspuru-Guzik, Finding low-energy conformations of lattice protein models by quantum annealing. *Sci. Rep.* **2**, 571 (2012). Medline doi:10.1038/srep00571

37. C. C. McGeoch, C. Wang, *Proceedings of the ACM International Conference on Computing Frontiers*, CF '13 (ACM, New York, NY, USA, 2013), pp. 23:1–23:11.

38. D. Venturelli *et al*., *Phys. Rev. X* **5**, 031040 (2015).

39. D. Venturelli, D. J. J. Marchand, G. Rojo, *arXiv:1506.08479* (2015).

40. V. S. Denchev *et al*., *arXiv:1512.02206* (2015).

41. Z. Bian *et al*., *arXiv:1603.03111* (2016).

42. S. Mandra, Z. Zhu, W. Wang, A. Perdomo-Ortiz, H. G. Katzgraber, *arXiv:1604.01746* (2016).

43. D. Maruo, S. Utsunomiya, Y. Yamamoto, Truncated Wigner theory of coherent Ising machines based on degenerate optical parametric oscillator network. *Phys. Scr.* **91**, 083010 (2016). doi:10.1088/0031-8949/91/8/083010

44. R. Hamerly *et al*., *arXiv:1605.08121* (2016).

45. D. F. Walls, G. J. Milburn, *Quantum Optics* (Springer-Verlag, Berlin, 2008), second edn.

46. D. T. Pegg, S. M. Barnett, *J. Mod. Opt.* **44**, 225 (1997).

47. P. Alimonti, V. Kann, *Algorithms and Complexity*, G. Bongiovanni, D. P. Bovet, G. D. Battista, eds., no. 1203 in Lecture Notes in Computer Science (Springer Berlin Heidelberg, 1997), pp. 288–298. DOI: 10.1007/3-540-62592-5_80.

48. J. Sima, S. E. Schaeffer, *arXiv:cs/0506100* (2005).

49. B. Bollobás, A Probabilistic Proof of an Asymptotic Formula for the Number of Labelled Regular Graphs. *Eur. J. Combin.* **1**, 311–316 (1980). doi:10.1016/S0195-6698(80)80030-8

50. N. C. Wormald, *Surveys in combinatorics*, J. D. Lamb, D. A. Preece, eds., London Math. Soc. Lecture Note Series (Canterbury, 1999), pp. 239–298.

51. G. Bounova, Topological evolution of networks: case studies in the US airlines and language Wikipedias, Ph.D. Thesis, Massachusetts Institute of Technology (2009).

52. M. Yamaoka *et al*., *2015 IEEE International Solid-State Circuits Conference (ISSCC)* (2015), pp. 1–3.

53. Y. Okawachi, M. Yu, K. Luke, D. O. Carvalho, S. Ramelow, A. Farsi, M. Lipson, A. L. Gaeta, Dual-pumped degenerate Kerr oscillator in a silicon nitride microresonator. *Opt. Lett.* **40**, 5267–5270 (2015). Medline doi:10.1364/OL.40.005267

54. P. C. Humphreys, B. J. Metcalf, J. B. Spring, M. Moore, X. M. Jin, M. Barbieri, W. S. Kolthammer, I. A. Walmsley, Linear optical quantum computing in a single spatial mode. *Phys. Rev. Lett.* **111**, 150501 (2013). Medline doi:10.1103/PhysRevLett.111.150501

55. S. Aaronson, A. Arkhipov, *Proceedings of the Forty-third Annual ACM Symposium on Theory of Computing*, STOC '11 (ACM, New York, NY, USA, 2011), pp. 333–342.

56. Y. He *et al*., *arXiv:1603.04127* (2016).

57. J. Huh, G. G. Guerreschi, B. Peropadre, J. R. McClean, A. Aspuru-Guzik, Boson sampling for molecular vibronic spectra. *Nat. Photonics* **9**, 615–620 (2015). doi:10.1038/nphoton.2015.153

58. U. L. Andersen, T. Gehring, C. Marquardt, G. Leuchs, 30 years of squeezed light generation. *Phys. Scr.* **91**, 053001 (2016). doi:10.1088/0031-8949/91/5/053001